

---

# EXAONEPath 1.0 Patch-level Foundation Model for Pathology

---

**Juseung Yun ,Yi Hu, Jinhyung Kim, Jongseong Jang & Soonyoung Lee**  
LG AI Research  
Seoul, South Korea  
{js.yun ,Yi Hu, Jinhyung.Kim, j.jang, soonyoung.lee}@lgresearch.ai

## Abstract

Recent advancements in digital pathology have led to the development of numerous foundational models that utilize self-supervised learning on patches extracted from gigapixel whole slide images (WSIs). While this approach leverages vast amounts of unlabeled data, we have discovered a significant issue: features extracted from these self-supervised models tend to cluster by individual WSIs, a phenomenon we term WSI-specific feature collapse. This problem can potentially limit the model's generalization ability and performance on various downstream tasks. To address this issue, we introduce EXAONEPath<sup>1</sup>, a novel foundational model trained on patches that have undergone stain normalization. Stain normalization helps reduce color variability arising from different laboratories and scanners, enabling the model to learn more consistent features. EXAONEPath is trained using 285,153,903 patches extracted from a total of 34,795 WSIs. Our experiments demonstrate that EXAONEPath significantly mitigates the feature collapse problem, indicating that the model has learned more generalized features rather than overfitting to individual WSI characteristics. We compared EXAONEPath with state-of-the-art models across six downstream task datasets, and our results show that EXAONEPath achieves superior performance relative to the number of WSIs used and the model's parameter count. This suggests that the application of stain normalization has substantially improved the model's efficiency and generalization capabilities.

## \*Important Notice\*

This document is valid only for EXAONEPath version 1.0. Also, please refer to the license at the end of the document, when using this model.

## 1 Introduction

In modern pathology, the analysis of digital pathology images plays a crucial role in cancer subtyping [Lu et al., 2021, Shao et al., 2021], prognosis prediction [Mobadersany et al., 2018, Chen et al., 2022b, Shmatko et al., 2022], and quantifying the tissue microenvironment [Schapiro et al., 2017, Mahmood et al., 2018, Saltz et al., 2018a, Graham et al., 2019]. Whole Slide Images (WSIs), in particular, are high-resolution digitized tissue slides that often measure tens of thousands by tens of thousands of pixels in size. Due to the vast dimensions of these WSIs, many researchers have adopted the approach of dividing the images into smaller patches to train their models. A single WSI can be divided into thousands or even tens of thousands of patches, but accurately labeling each of these patches is a significant burden in terms of time and cost. To overcome this limitation, recent approaches have

---

<sup>1</sup> github:<https://github.com/LG-AI-EXAONE/EXAONEPath>  
huggingface:<https://huggingface.co/LGAI-EXAONE/EXAONEPath>

widely adopted self-supervised learning techniques to first train a foundation model, which is then fine-tuned for various downstream tasks [Kang et al., 2023, Chen et al., 2024, Vorontsov et al., 2023, Dippel et al., 2024]. This approach allows for the effective utilization of large amounts of unlabeled data while achieving high performance with limited labeled data.

In this paper, we first introduce our novel observation that the features of models trained through self-supervised learning exhibit an unexpectedly high degree of overlap. Specifically, we divide whole slide images into patches and create a foundation model using the DINO (self-Distillation with NO labels) [Caron et al., 2021] self-supervised learning method. During this process, as the whole slides are divided into small patches for training, the model has no information about which whole slide each specific patch originated from. Subsequently, we extract features of each patch and visualize them using t-SNE [van der Maaten and Hinton, 2008]. Surprisingly, we observe that the patch features cluster according to their respective WSIs. We refer to this phenomenon as WSI-specific feature collapse. Whole slides undergo Hematoxylin and Eosin (H&E) staining to clearly reveal tissue structures. We hypothesize that this clustering phenomenon occurs due to variations in staining intensity between laboratories or even within the same laboratory, resulting in color differences among WSIs. In whole slide image analysis, model features should focus on capturing pathologically significant information rather than simply relying on the degree of staining. Critical information that should be observed includes nuclear size and shape, cell density, and structural changes in tissue. If the model concentrates excessively on staining variations, it may overlook these essential pathological features, potentially leading to inaccuracies in important downstream tasks such as cancer type classification, mutation classification, and survival analysis. Therefore, it is crucial to ensure that the model is trained to properly recognize and learn these important pathological characteristics during the training process. To address this issue, we first apply Macenko normalization [Macenko et al., 2009] to the patches before feature extraction in an effort to standardize the color characteristics across patches. While this somewhat mitigates the feature collapse, significant collapse is still observed. To further address this challenge, we introduce EXAONEPath, a stain-normalized pathology foundation model. This model is created by performing DINO self-supervised learning pretraining on patches that have undergone Macenko normalization. EXAONEPath is trained using 285,153,903 patches extracted from a total of 34,795 WSIs. We have confirmed that EXAONEPath significantly mitigates the feature collapse problem. This implies that the model has a higher potential to extract pathologically relevant features crucial for downstream tasks, rather than simply relying on color-based characteristics. These improvements are expected to enhance the model’s performance and reliability across various pathological analysis tasks. We validated the performance of EXAONEPath on various patch-level tasks including PCAM [Veeling et al., 2018, Bejnordi et al., 2017], MHIST [Wei et al., 2021], CRC 100k [Kather et al., 2018], TIL-Detection [Abousamra et al., 2022, Saltz et al., 2018b, Kaczmarzyk et al.], MSI-CRC, and MSI-STAD [Kather, 2019] dataset. Notably, despite being trained on relatively less data compared to existing State-of-the-Art (SOTA) models, and using only publicly available datasets, EXAONEPath achieved comparable performance levels to these SOTA models across these diverse tasks. Our contributions can be summarized as follows:

- We discover and analyze the ‘WSI-specific feature collapse’ phenomenon, where patch features cluster according to their source WSI, despite the foundation model being trained without information about which WSI each patch was extracted from.
- To address this issue, we develop EXAONEPath, a novel model that applies stain normalization to patches during foundation model training. We demonstrate that EXAONEPath effectively mitigates the feature collapse problem.
- We evaluate EXAONEPath against state-of-the-art models on six diverse patch-level tasks. The results show that EXAONEPath exhibits superior performance relative to the number of WSIs used and the number of model parameters.

## 2 Related Work

In this section, we briefly overview some relevant literature.

**Pathology Image Foundation Models.** With the significant advancements in self-supervised learning (SSL) methods, there is a notable trend in applying these methods, commonly used in natural image processing, to histopathology to develop robust foundation models for whole slide images (WSIs) [Gildenblat and Klaiman, 2019, Ciga et al., 2022, Yang et al., 2022, Kang et al., 2023]. Given the

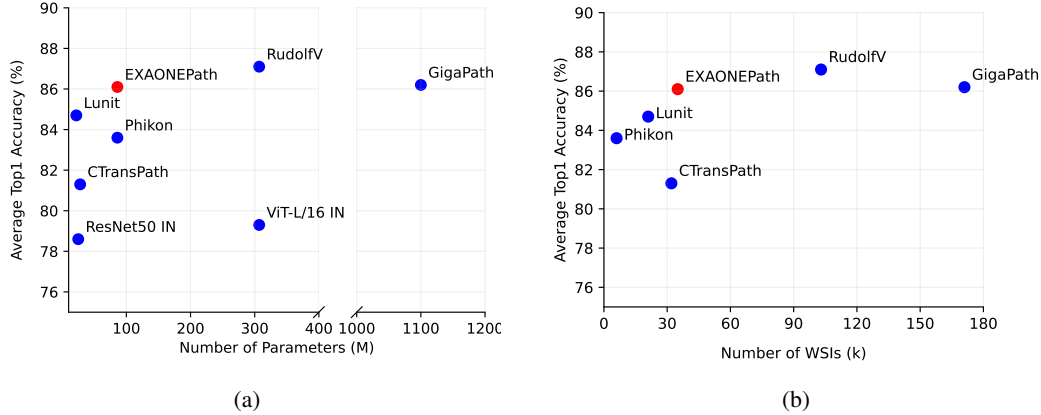


Figure 1: **Performance comparison of models based on the number of parameters and the number of WSIs used for training.** The average Top-1 accuracy represents the mean linear evaluation performance across six downstream tasks. (a) Average Top-1 accuracy versus the number of parameters. (b) Average Top-1 accuracy versus the number of WSIs used for training. Notably, our model (EXAONEPath) achieves high performance despite having fewer parameters and using fewer WSIs compared to other models, demonstrating its efficiency.

gigapixel resolution of WSIs, creating foundation models by dividing images into patch units has become a prevalent approach. For example, REMEDIS [Azizi et al., 2023] employs SimCLR [Chen et al., 2020a] to train on various medical domain images, including pathology. Similarly, Ciga et al. [2022] utilizes SimCLR for training on histopathology images. Kang et al. [2023] applies four SSL methods—MoCo v2 [Chen et al., 2020b], SwAV [Caron et al., 2020], Barlow Twins [Zbontar et al., 2021], and DINO [Caron et al., 2021]—to pathology data and evaluates their performance on image classification and nuclei instance segmentation tasks. Campanella et al. [2023] compares the Masked Autoencoder (MAE) [He et al., 2022] and DINO [Caron et al., 2021] algorithms using the largest pathology dataset to date, which comprises over three billion images. Their evaluation across six clinical tasks demonstrates that pre-training on pathology data is more effective than pre-training on natural images, with the DINO algorithm showing superior generalization performance across all tasks. HIPT [Chen et al., 2022a] also implements DINO within a hierarchical structure. Phikon [Filiot et al., 2023] employs iBOT [Zhou et al., 2022], a self-supervised learning method based on masked image modeling (MIM), for histology images. The ViT-Base model using iBOT exhibits excellent performance across 17 downstream tasks on 7 cancer types, suggesting its potential for developing a foundation model for histopathology. CTransPath [Wang et al., 2022] introduces a new self-supervised learning strategy called Semantically-Relevant Contrastive Learning (SRCL), an enhancement of MoCo v3 [Chen\* et al., 2021]. Additionally, UNI [Chen et al., 2024], RudolfV [Dippel et al., 2024], Virchow [Vorontsov et al., 2023], and Prov-GigaPath [Xu et al., 2024] utilize DINO v2 for training pathology foundation models. Prov-GigaPath [Xu et al., 2024] applies the LongNet [Ding et al., 2023] architecture to learn slide-level representations.

To our knowledge, none of these studies utilizing self-supervised learning for developing pathology foundation models employ stain normalization on the training data. In contrast, we incorporate stain normalization in our training process, which we believe offers significant advantages for learning robust foundation models.

**Stain Normalization.** Stain normalization is a critical process in histopathology designed to address the inconsistencies in color that arise from staining protocols, device properties, scanner settings, and tissue preparation methods. These variations can affect the accuracy of automated diagnostic systems. Therefore, robust methods to standardize the appearance of histopathological images are essential to ensure reliable and reproducible analyses.

Early methods focused on histogram transformation, such as Reinhard normalization [Reinhard et al., 2001], which employs statistical techniques to transfer the color characteristics from one image to another by converting them to the Lab color space. This method is widely recognized for its simplicity and effectiveness in standardizing color distributions across different images.

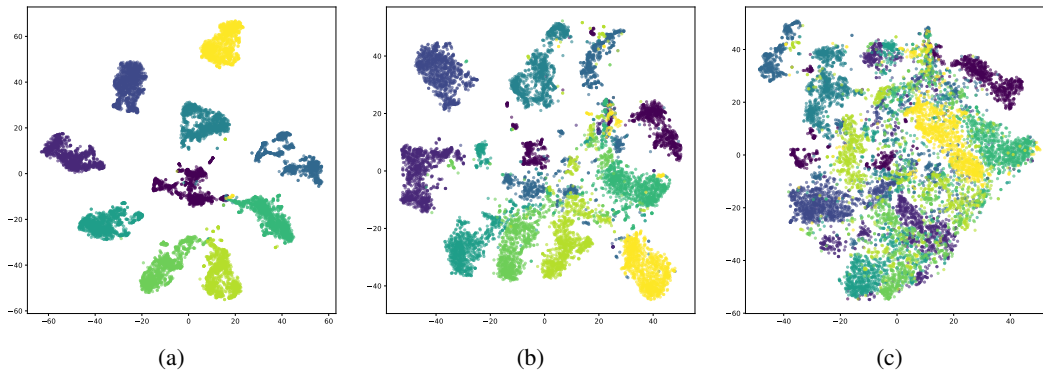


Figure 2: **t-SNE visualization of features extracted from a foundation model trained with DINO.** 1000 patches are randomly sampled from each of 10 arbitrarily selected WSIs, and the features from each of the 10 WSIs are represented in different colors. Despite having no information about the source WSI for each patch, the model exhibits WSI-specific feature collapse, where features tend to cluster by WSI. (a) Features obtained by inputting patches without any stain normalization into a model trained on non-stain-normalized images, showing severe feature collapse. (b) Features obtained by inputting stain-normalized patches into a model trained on non-stain-normalized images, showing significant but reduced collapse compared to (a). (c) Features obtained by inputting stain-normalized patches into a model trained on stain-normalized images, showing significantly reduced feature collapse, as proposed by our method.

Another notable approach is Macenko normalization [Macenko et al., 2009], which transforms images into an optical density (OD) space. PCA is then performed on the OD space to identify the principal components corresponding to the Hematoxylin and Eosin stains, thus enabling effective stain separation and normalization. Inspired by the biological fact about stain binding, Vahadane et al. [2016] extended the use of nonnegative matrix factorization (NMF) [Rabinovich et al., 2003] by introducing sparsity constraints, which enhance the robustness of stain separation by limiting the number of non-zero components, thereby aligning with the actual biological composition of histological samples.

Recently, deep learning-based approaches have advanced stain normalization techniques, particularly through the use of image-to-image translation architectures combined with adversarial learning methods [Bentaieb and Hamarneh, 2018]. These approaches leverage generative adversarial networks (GANs) [Goodfellow et al., 2014], such as CycleGAN [Zhu et al., 2017] and StarGAN [Choi et al., 2018], to learn the mappings between different staining styles. By employing adversarial training, these models are able to produce normalized images that closely resemble the target staining characteristics while preserving essential structural features of the tissue [Wagner et al., 2021, Nazki et al., 2023]. Such advancements demonstrate the potential of deep learning to overcome the limitations of traditional stain normalization methods, offering more robust and scalable solutions for digital pathology.

### 3 Self-supervised Pre-training for Pathology

This section introduces the ‘WSI-specific feature collapse’ that occurs when pathology foundation models are trained using self-supervised learning, and discusses methods to reduce this phenomenon. In Section 3.1, we discuss the ‘WSI-specific feature collapse’ problem. This refers to the phenomenon where features from the same WSI tend to cluster together, even though each patch is learned without information about which WSI it comes from during the training process. Section 3.2 demonstrates that applying stain normalization before feature extraction does not significantly reduce the collapse. In Section 3.3, we introduce EXAONEPath, which applies stain normalization to the training data from the beginning of foundation model training to further reduce ‘WSI-specific feature collapse’.

### 3.1 motivation: wsi specific feature collapse

DINO [Caron et al., 2021] involves applying different augmentations to an image and inputting them into both teacher and student models, training them to produce identical features. Color jittering is a data augmentation technique commonly used in self-supervised learning, including DINO. It involves randomly altering the colors of an image to create different variations, helping the model learn robust features invariant to color changes. However, despite the use of color jittering augmentation, when visualizing patch features using t-SNE [van der Maaten and Hinton, 2008], we observe that features still tend to collapse according to their source WSI. Specifically, we trained a foundation model using DINO on  $256^2$ -sized patches extracted from gigapixel WSIs. It is important to note that the neural network is trained only on these isolated patches, without any information about which WSI each patch originated from. We randomly selected 1,000 patches from each of 10 arbitrary WSIs, performed a forward pass through the trained foundation model, and then visualized the resulting 10,000 features using t-SNE (see Figure 2a). Interestingly, even though the model does not know the source WSI of each patch, we observe that patches from the same WSI tend to have similar features and cluster together. This phenomenon suggests that, instead of learning features crucial for downstream tasks and pathologically significant, the model may have unintentionally learned WSI-specific characteristics, such as staining intensity or subtle differences due to scanner variations. This feature collapse phenomenon could potentially compromise the model’s ability to generalize. If the model becomes overly adapted to individual WSI characteristics, its performance may degrade when applied to new WSIs or images acquired from different institutions. This result suggests that when creating a pretrained foundation model for WSIs, rather than directly applying self-supervised learning methods used for natural images, we need to use approaches that take into account the specific characteristics of WSIs.

### 3.2 stain normalization

We hypothesized that the WSI-specific feature collapse occurs due to variations in staining intensity across different WSIs, which result in color differences. This phenomenon arises from the staining process of WSIs, which depends on the types of stains used and the degree of staining. Additionally, differences in slide scanner settings or performance can affect color variations in digitized WSIs. Therefore, to address these color differences, we employed Macenko stain normalization [Macenko et al., 2009] before extracting features. We used the same pretrained model and patches as described in Section 3.1. Figure 2b shows the results. Compared to Figure 2a, where features are completely separated by WSI, Figure 2b shows that features from different WSIs are now slightly mixed, but they still tend to cluster by WSI. This indicates that while Macenko normalization partially mitigates color differences between WSIs, it is not sufficient to fully resolve the issue, as features from the same WSI still exhibit noticeable clustering and the collapse problem remains significant. Furthermore, it suggests that applying Macenko normalization only during inference has limited effectiveness because the pretrained model has already learned to extract features biased toward color characteristics.

### 3.3 stain normalized whole slide pathology image foundation model

We use DINO [Caron et al., 2021] self-supervised learning to train a WSI foundation model. We refer to this model as EXAONEPath, which is trained with stain-normalized data using DINO. DINO involves applying different augmentations to an image and inputting them into both teacher and student models, training them to produce identical features. The teacher model, updated with an exponential moving average (EMA) of the student parameters, guides the output of the student model. The student model is trained using cross-entropy loss to measure their similarity. By inputting differently augmented images into the teacher and student models, the features produced by both models are compared and aligned. In the original DINO paper, different augmentation methods are applied to two  $256^2$  global views and several  $96^2$  local views of each image.

Combining Macenko normalization with the existing DINO augmentation is a design choice. We apply Macenko normalization to all images with 100% probability before applying DINO augmentation. This approach is chosen because applying Macenko normalization to each global view and local view individually is computationally intensive, creating a bottleneck in the data loader during training. Figure 2c visualizes the features of EXAONEPath trained with DINO using Macenko-normalized images. Macenko normalization is applied not only during training but also when extracting features for each patch in the visualization process. Compared to Figures 2a and 2b, we observe that patch

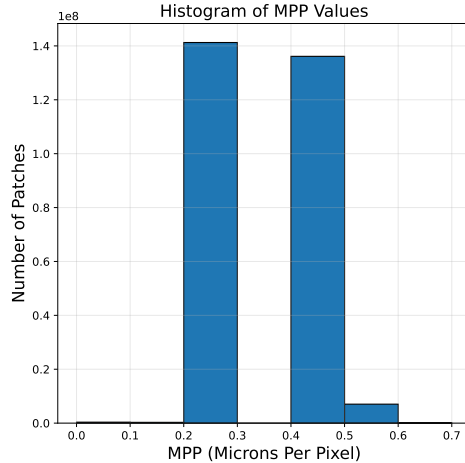


Figure 3: **MPP distribution of the training data.** Most of the data used for training is concentrated around 0.25 MPP and 0.5 MPP.

features from various WSIs are much more intermingled. This indicates that the model learns more generalized features and is less dependent on the source of the WSIs. This allows the model to focus on more histologically relevant features. We still observe that some clusters of features are grouped by WSI. We believe this occurs for two reasons: first, while Macenko normalization significantly reduces color differences, it may not completely eliminate them; second, patches from the same WSI likely share clinically relevant features beyond just color, due to variations in tissue type, cancer subtype, and patient characteristics within each WSI.

## 4 Experiments

In this section, we describe the experimental settings and results. Section 4.1 provides a detailed explanation of the data used for pretraining the whole slide image foundation model. Section 4.2 offers comprehensive information on the pretraining methodology. Section 4.3 describes the data for the downstream tasks we aim to evaluate. Section 4.4 explains in detail the methods used to training the downstream tasks. Finally, Section 4.5 presents the results of the linear evaluation on the downstream tasks.

### 4.1 pretraining data

We collected 34,795 Formalin-Fixed, Paraffin-Embedded (FFPE) Hematoxylin and Eosin (H&E) stained whole slide images (WSIs). Following CLAM [Lu et al., 2021], we divide the WSIs into non-overlapping patches, focusing only on the tissue-containing regions. Given that each WSI has a different micron per pixel (MPP), we adjust the patch sizes so that they correspond to 0.5 MPP when resized to  $256^2$ . For instance, for WSIs with 0.25 MPP, we extract patches at  $512^2$  dimensions, and for WSIs with 0.5 MPP, we extract patches at  $256^2$  dimensions. However, for training the EXAONEPath model, the patches are not resized to achieve a uniform 0.5 MPP. Instead, we retain the original patch sizes during training because the DINO algorithm’s input image transform includes random resized cropping. Even if we resize the patches to 0.5 MPP, the model’s input would still undergo changes in MPP due to this random resized crop operation. Therefore, maintaining the originally extracted patch sizes allows us to preserve the maximum amount of information from each WSI while relying on DINO’s augmentations to introduce the necessary variability in scale and perspective. Figure 3 presents the distribution of MPP values for patches extracted from the WSIs. Most of the data used for training is concentrated around 0.25 MPP and 0.5 MPP. The total number of patches used for training EXAONEPath is 285,153,903.

## 4.2 pretraining details

We train EXAONEPath using DINO [Caron et al., 2021] with a ViT-B model [Dosovitskiy et al., 2021], which has a patch size of 16, initializing the weights with those pretrained on the ImageNet dataset [Russakovsky et al., 2015]. Training is conducted on 10 machines, each equipped with 8 A100 GPUs. We use a batch size of 5,120 and a learning rate of 0.005, training the model for 10 epochs. The learning rate is warmed up over the first 1,000 iterations. We employ bfloat16 precision training. The output layer is not fixed; instead, it is trained from scratch. Additionally, we set the number of local crops to 8. Other hyperparameters follow the settings from the original DINO paper for training the ViT-B model.

## 4.3 downstream task data

We evaluate EXAONEPath on six publicly available patch-level datasets for classification tasks: PCAM [Veeling et al., 2018, Bejnordi et al., 2017], MHIST [Wei et al., 2021], CRC-100K [Kather et al., 2018], TIL Detection [Abousamra et al., 2022, Saltz et al., 2018b, Kaczmarzyk et al.], MSI CRC [Kather, 2019], and MSI STAD [Kather, 2019].

**PCAM** [Veeling et al., 2018, Bejnordi et al., 2017] consists of 327,680 color images, each of  $96^2$  pixels, extracted from histopathologic scans of lymph node sections, and each annotated with a binary label indicating the presence of metastatic tissue. The dataset is divided into a training set of 262,144 examples and validation and test sets of 32,768 examples each, with no overlap between WSIs across splits. All splits maintain a 50/50 balance between positive and negative examples. A positive label indicates the presence of at least one pixel of tumor tissue within the central  $32^2$  pixel region of a patch, while tumor tissue in the outer region does not affect the label. PCAM is derived from the Camelyon16 Challenge, which includes 400 H&E-stained WSIs of sentinel lymph node sections, digitized at 40x magnification (0.243 MPP) and undersampled to 10x for a larger field of view. The dataset follows the train/test split from Camelyon16, with 20% of the training WSIs held out for validation.

**MHIST** [Wei et al., 2021] consists of 3,152 H&E-stained FFPE images, each  $224^2$  pixels in size, of colorectal polyps, collected from the Department of Pathology and Laboratory Medicine at Dartmouth-Hitchcock Medical Center (DHMC). Each image is scanned at 40x magnification and resized to 8x magnification and is labeled based on the consensus of seven pathologists at DHMC, categorizing the type of colorectal polyps. The MHIST dataset focuses on a binary classification task, distinguishing between Hyperplastic Polyps (HP) and Sessile Serrated Adenomas (SSA). The dataset is divided into training and test sets, with the training set further split into training and validation sets using an 80:20 ratio. This results in 1,740 training samples, 435 validation samples, and 977 test samples.

**CRC-100K** [Kather et al., 2018] consists of 100,000 non-overlapping image patches ( $224^2$  pixels, 0.5 MPP) from H&E-stained histological images of human colorectal cancer (CRC) and normal tissue. The dataset includes both color-normalized images using Macenko’s method, and non-normalized images, with the latter exhibiting slight variations in staining intensity and color. We utilize the non-normalized images for our work, as we intend to apply Macenko normalization using our Macenko target image. Tissue classes include Adipose (ADI), Background (BACK), Debris (DEB), Lymphocytes (LYM), Mucus (MUC), Smooth Muscle (MUS), Normal Colon Mucosa (NORM), Cancer-associated Stroma (STR), and Colorectal Adenocarcinoma Epithelium (TUM). These patches are manually extracted from 86 H&E-stained FFPE samples from the NCT Biobank and the UMM pathology archive. An additional set, CRC-VAL-HE-7K, consists of 7,180 patches from 50 patients with CRC and serves as a validation set with no overlap with the original dataset. Since there is no separate test set provided, we use CRC-VAL-HE-7K as our test set. For training and validation, we split the original training set into an 80:20 ratio to create training and validation sets.

**TIL Detection** [Abousamra et al., 2022, Saltz et al., 2018b, Kaczmarzyk et al.] dataset consists of 304,097 H&E-stained images, each  $100^2$  pixels at 0.5 MPP, extracted from FFPE sections covering 23 different cancer types from TCGA [Weinstein et al., 2013]. The dataset is used for predicting TIL-positive images, where an image is considered positive if it contains more than two tumor-infiltrating lymphocytes (TILs). The dataset is divided into 209,221 training images, 38,601 validation images, and 56,275 test images. Each image is annotated as either TIL-positive (54,910 images) or TIL-negative (249,187 images), based on the presence of at least two TILs.

Table 1: **Linear evaluation performance on six downstream tasks.** EXAONEPath is compared with other models, including state-of-the-art pathology foundation models. Top-1 accuracy is shown. Values for models other than GigaPath are taken from the RudolfV paper

Model	# data		# of params	Dataset						
	WSI	Patch		PCAM	MHIST	CRC-100K	TIL Det.	MSI CRC	MSI STAD	Avg
ResNet50 ImageNet	-	-		0.833	0.806	0.849	0.915	0.653	0.664	0.786
ViT-L/16 ImageNet	-	-	307M	0.852	0.796	0.847	0.924	0.669	0.671	0.793
Lunit	21k	33M	22M	0.918	0.771	0.949	0.943	0.745	0.756	0.847
CTransPath	32k	15M	28M	0.872	0.817	0.840	0.930	0.694	0.726	0.813
Phikon	6k	43M	86M	0.906	0.795	0.883	<b>0.946</b>	0.733	0.751	0.836
Virchow	1.5M	2B	632M	0.933	<b>0.834</b>	0.968	-	-	-	-
RudolfV	103k	759M	307M	0.944	0.821	<b>0.973</b>	0.943	0.755	0.788	<b>0.871</b>
GigaPath (patch encoder)	171k	1.3B	1,100 M	<b>0.947</b>	0.822	0.964	0.938	0.753	0.748	0.862
EXAONEPath (ours)	35k	285M	86M	0.901	0.818	0.946	0.939	<b>0.756</b>	<b>0.804</b>	0.861

**MSI CRC** and **MSI STAD** [Kather, 2019]. For MSI CRC, the training set contains 93,408 image patches, and the test set comprises 99,904 image patches. For MSI STAD, the training set includes 100,570 image patches, and the test set contains 118,008 image patches. All images are  $224^2$  pixels at 0.5 MPP and are derived from histological images of colorectal and gastric cancer patients in the TCGA cohort. The images are sourced from FFPE diagnostic slides. Preprocessing includes automatic tumor detection, resizing to  $224^2$  pixels, and color normalization using Macenko’s method. Patients are categorized into "MSS" (microsatellite stable) or "MSIMUT" (microsatellite instable or highly mutated) groups, and the data is split into training (70%) and testing (30%) sets at the patient level, with the training set balanced by undersampling excess MSS tiles. We further split the training set into training and validation sets with an 80:20 ratio.

#### 4.4 Downstream Task Training Details

We use linear evaluation, a common practice in previous SSL research for evaluation [Chen et al., 2020a, Zbontar et al., 2021, He et al., 2020]. Training is performed using the SGD optimizer with a learning rate of 0.1, without weight decay, and a momentum of 0.9, with a batch size of 128 for 12,500 iterations. The images are first resized to  $256^2$  pixels and then center-cropped to  $224^2$  pixels. No additional data augmentation is applied. Macenko normalization is used in both the training and evaluation processes. Even datasets that are already Macenko-normalized are re-normalized using the same Macenko target images employed during EXAONEPath training.

#### 4.5 Downstream Task Results

Table 1 presents the classification accuracy results obtained from the linear evaluation. EXAONEPath demonstrated competitive performance, achieving an average accuracy of 0.861 across the six downstream tasks. Notably, EXAONEPath achieves the highest performance among all models on the MSI CRC dataset, with an accuracy of 0.756, and on the MSI STAD dataset, with an accuracy of 0.804. Figure 1a compares the number of model parameters with the average accuracy across the six downstream tasks. Models positioned in the top left have fewer parameters and higher accuracy, indicating better efficiency. EXAONEPath exhibits parameter efficiency compared to other models. Figure 1b shows the average accuracy across six downstream tasks in relation to the number of WSIs used for model training. Models in the top left exhibit higher accuracy with fewer WSIs used for training. Training with stain-normalized images effectively mitigates the WSI-specific feature collapse problem, allowing for strong performance with fewer data and relatively smaller models.

## 5 Conclusion

In this paper, we have made a notable discovery during the visualization of features from patches extracted from models trained with self-supervised learning. We have termed this phenomenon ‘WSI-specific feature collapse’, where features from patches extracted from the same Whole Slide Image (WSI) tend to cluster together. This suggests inefficient learning, as it leads to the extraction of similar features when thousands of patches are derived from a single WSI. We hypothesized that this phenomenon arose from the substantial color variations between different WSIs. To address this issue, we utilized Macenko normalization on the training data to minimize color differences



and developed EXAONEPath. As a result, EXAONEPath significantly reduced the WSI-specific feature collapse and achieved comparable or superior performance to existing models, even though those models use more data and parameters. However, despite the considerable improvement in mitigating WSI-specific feature collapse through EXAONEPath, this phenomenon appears to persist to some extent. This suggests the need for further research. Specifically, developing more effective and computationally efficient stain normalization techniques, suitable for integration into data loaders, could be a promising direction for future research. Additionally, exploring new learning methods or model architectures that can more effectively prevent feature collapse is also necessary. In conclusion, EXAONEPath represents significant progress in WSI analysis, laying the groundwork for more efficient and accurate pathological image analysis.

## References

- Shahira Abousamra, Rajarsi Gupta, Le Hou, Rebecca Batiste, Tianhao Zhao, Anand Shankar, Arvind Rao, Chao Chen, Dimitris Samaras, Tahsin Kurc, et al. Deep learning-based mapping of tumor infiltrating lymphocytes in whole slide images of 23 types of cancer. *Frontiers in oncology*, 11: 806603, 2022.
- Shekoofeh Azizi, Laura Anne Culp, Jan Freyberg, Basil Mustafa, Sebastien Baur, Simon Kornblith, Ting Chen, Patricia MacWilliams, Sara Mahdavi, Ellery Wulczyn, Boris Babenko, Megan Zoë Walker, Aaron Loh, Cameron Chen, Yuan Liu, Pinal Bavishi, Scott Mayer McKinney, Jim Winkens, Abhijit Guha Roy, Zach William Beaver, Fiona Keleher Ryan, Justin David Krogue, Mozziyar Etemadi, Umesh Telang, Yun Liu, Lily Hao Yi Peng, Greg Corrado, Dale Richard Webster, David James Fleet, Geoffrey Everest Hinton, Neil Houlsby, Alan Karthikesalingam, Mohammad Norouzi, and Vivek Natarajan. Robust and data-efficient generalization of self-supervised machine learning for diagnostic imaging. *Nature Biomedical Engineering*, 2023. URL <https://rdcu.be/dd4M9>.
- Babak Ehteshami Bejnordi, Mitko Veta, Paul Johannes Van Diest, Bram Van Ginneken, Nico Karssemeijer, Geert Litjens, Jeroen AWM Van Der Laak, Meyke Hermsen, Quirine F Manson, Maschenka Balkenhol, et al. Diagnostic assessment of deep learning algorithms for detection of lymph node metastases in women with breast cancer. *Jama*, 318(22):2199–2210, 2017.
- Aïcha Bentaieb and G. Hamarneh. Adversarial stain transfer for histopathology image analysis. *IEEE Transactions on Medical Imaging*, 37:792–802, 2018. URL <https://api.semanticscholar.org/CorpusID:3668673>.
- Gabriele Campanella, Ricky Kwan, Eugene Fluder, Jennifer Zeng, Aryeh Stock, Brandon Veremis, Alexandros D Polydorides, Cyrus Hedvat, Adam Schoenfeld, Chad Vanderbilt, et al. Computational pathology at health system scale—self-supervised foundation models from three billion images. *arXiv preprint arXiv:2310.07033*, 2023.
- Mathilde Caron, Ishan Misra, Julien Mairal, Priya Goyal, Piotr Bojanowski, and Armand Joulin. Unsupervised learning of visual features by contrasting cluster assignments. *Advances in neural information processing systems*, 33:9912–9924, 2020.
- Mathilde Caron, Hugo Touvron, Ishan Misra, Hervé Jégou, Julien Mairal, Piotr Bojanowski, and Armand Joulin. Emerging properties in self-supervised vision transformers. In *Proceedings of the IEEE/CVF international conference on computer vision*, pages 9650–9660, 2021.
- Richard J Chen, Chengkuan Chen, Yicong Li, Tiffany Y Chen, Andrew D Trister, Rahul G Krishnan, and Faisal Mahmood. Scaling vision transformers to gigapixel images via hierarchical self-supervised learning. In *Proceedings of the IEEE/CVF Conference on Computer Vision and Pattern Recognition*, pages 16144–16155, 2022a.
- Richard J Chen, Ming Y Lu, Drew FK Williamson, Tiffany Y Chen, Jana Lipkova, Zahra Noor, Muhammad Shaban, Maha Shady, Mane Williams, Bumjin Joo, et al. Pan-cancer integrative histology-genomic analysis via multimodal deep learning. *Cancer Cell*, 40(8):865–878, 2022b.
- Richard J Chen, Tong Ding, Ming Y Lu, Drew FK Williamson, Guillaume Jaume, Bowen Chen, Andrew Zhang, Daniel Shao, Andrew H Song, Muhammad Shaban, et al. Towards a general-purpose foundation model for computational pathology. *Nature Medicine*, 2024.

- Ting Chen, Simon Kornblith, Mohammad Norouzi, and Geoffrey Hinton. A simple framework for contrastive learning of visual representations. In *International conference on machine learning*, pages 1597–1607. PMLR, 2020a.
- Xinlei Chen, Haoqi Fan, Ross Girshick, and Kaiming He. Improved baselines with momentum contrastive learning. *arXiv preprint arXiv:2003.04297*, 2020b.
- Xinlei Chen\*, Saining Xie\*, and Kaiming He. An empirical study of training self-supervised vision transformers. *arXiv preprint arXiv:2104.02057*, 2021.
- Yunjey Choi, Minje Choi, Munyoung Kim, Jung-Woo Ha, Sunghun Kim, and Jaegul Choo. StarGAN: Unified generative adversarial networks for multi-domain image-to-image translation. In *Proceedings of the IEEE Conference on Computer Vision and Pattern Recognition*, 2018.
- Ozan Ciga, Tony Xu, and Anne Louise Martel. Self supervised contrastive learning for digital histopathology. *Machine Learning with Applications*, 7:100198, 2022.
- Jiayu Ding, Shuming Ma, Li Dong, Xingxing Zhang, Shaohan Huang, Wenhui Wang, Nanning Zheng, and Furu Wei. Longnet: Scaling transformers to 1,000,000,000 tokens. *arXiv preprint arXiv:2307.02486*, 2023.
- Jonas Dippel, Barbara Feulner, Tobias Winterhoff, Simon Schallenberg, Gabriel Dernbach, Andreas Kunft, Stephan Tietz, Philipp Jurmeister, David Horst, Lukas Ruff, et al. Rudolfov: a foundation model by pathologists for pathologists. *arXiv preprint arXiv:2401.04079*, 2024.
- Alexey Dosovitskiy, Lucas Beyer, Alexander Kolesnikov, Dirk Weissenborn, Xiaohua Zhai, Thomas Unterthiner, Mostafa Dehghani, Matthias Minderer, Georg Heigold, Sylvain Gelly, Jakob Uszkoreit, and Neil Houlsby. An image is worth 16x16 words: Transformers for image recognition at scale. *ICLR*, 2021.
- Alexandre Filiot, Ridouane Ghermi, Antoine Olivier, Paul Jacob, Lucas Fidon, Alice Mac Kain, Charlie Saillard, and Jean-Baptiste Schiratti. Scaling self-supervised learning for histopathology with masked image modeling. *medRxiv*, pages 2023–07, 2023.
- Jacob Gildenblat and Eldad Klaiman. Self-supervised similarity learning for digital pathology. In *MICCAI Workshops*, 2019.
- Ian Goodfellow, Jean Pouget-Abadie, Mehdi Mirza, Bing Xu, David Warde-Farley, Sherjil Ozair, Aaron Courville, and Yoshua Bengio. Generative adversarial nets. In *Advances in neural information processing systems*, pages 2672–2680, 2014.
- Simon Graham, Quoc Dang Vu, Shan E Ahmed Raza, Ayesha Azam, Yee Wah Tsang, Jin Tae Kwak, and Nasir Rajpoot. Hover-net: Simultaneous segmentation and classification of nuclei in multi-tissue histology images. *Medical image analysis*, 58:101563, 2019.
- Kaiming He, Haoqi Fan, Yuxin Wu, Saining Xie, and Ross Girshick. Momentum contrast for unsupervised visual representation learning. In *Proceedings of the IEEE/CVF conference on computer vision and pattern recognition*, pages 9729–9738, 2020.
- Kaiming He, Xinlei Chen, Saining Xie, Yanghao Li, Piotr Dollár, and Ross Girshick. Masked autoencoders are scalable vision learners. In *Proceedings of the IEEE/CVF conference on computer vision and pattern recognition*, pages 16000–16009, 2022.
- JR Kaczmarzyk, S Abousamra, T Kurc, R Gupta, and J Saltz. Dataset for tumor infiltrating lymphocyte classification (304,097 image patches from tcga), 2022. URL <https://doi.org/10.5281>.
- Mingu Kang, Heon Song, Seonwook Park, Donggeun Yoo, and Sérgio Pereira. Benchmarking self-supervised learning on diverse pathology datasets. In *Proceedings of the IEEE/CVF Conference on Computer Vision and Pattern Recognition*, pages 3344–3354, 2023.
- Jakob Nikolas Kather. Histological images for msi vs. mss classification in gastrointestinal cancer, fpe samples, 2019. URL <https://doi.org/10.5281/zenodo.2530835>. Zenodo.

- Jakob Nikolas Kather, Niels Halama, and Alexander Marx. 100,000 histological images of human colorectal cancer and healthy tissue, April 2018. URL <https://doi.org/10.5281/zenodo.1214456>.
- Ming Y Lu, Drew FK Williamson, Tiffany Y Chen, Richard J Chen, Matteo Barbieri, and Faisal Mahmood. Data-efficient and weakly supervised computational pathology on whole-slide images. *Nature biomedical engineering*, 5(6):555–570, 2021.
- Marc Macenko, Marc Niethammer, James S Marron, David Borland, John T Woosley, Xiaojun Guan, Charles Schmitt, and Nancy E Thomas. A method for normalizing histology slides for quantitative analysis. In *2009 IEEE international symposium on biomedical imaging: from nano to macro*, pages 1107–1110. IEEE, 2009.
- Faisal Mahmood, Daniel Borders, Richard Chen, Gregory McKay, Kevan J. Salimian, Alexander Baras, and Nicholas J. Durr. Adversarial training for multi-organ nuclei segmentation in computational pathology images. *IEEE Transactions on Medical Imaging*, 37(8):1940–1950, 2018. doi: 10.1109/TMI.2018.2820199.
- Pooya Mobadersany, Safoora Yousefi, Mohamed Amgad, David A Gutman, Jill S Barnholtz-Sloan, José E Velázquez Vega, Daniel J Brat, and Lee AD Cooper. Predicting cancer outcomes from histology and genomics using convolutional networks. *Proceedings of the National Academy of Sciences*, 115(13):E2970–E2979, 2018.
- Haseeb Nazki, Ognjen Arandjelovic, In Hwa Um, and David Harrison. Multipathgan: Structure preserving stain normalization using unsupervised multi-domain adversarial network with perception loss. In *Proceedings of the 38th ACM/SIGAPP Symposium on Applied Computing, SAC '23*, page 1197–1204, New York, NY, USA, 2023. Association for Computing Machinery. ISBN 9781450395175. doi: 10.1145/3555776.3578612. URL <https://doi.org/10.1145/3555776.3578612>.
- A. Rabinovich, S. Agarwal, C. A. Laris, J. H. Price, and S. Belongie. Unsupervised color decomposition of histologically stained tissue samples. In *Proceedings of the 16th International Conference on Neural Information Processing Systems, NIPS'03*, page 667–674, Cambridge, MA, USA, 2003. MIT Press.
- E. Reinhard, M. Adhikhmin, B. Gooch, and P. Shirley. Color transfer between images. *IEEE Computer Graphics and Applications*, 21(5):34–41, 2001. doi: 10.1109/38.946629.
- Olga Russakovsky, Jia Deng, Hao Su, Jonathan Krause, Sanjeev Satheesh, Sean Ma, Zhiheng Huang, Andrej Karpathy, Aditya Khosla, Michael Bernstein, et al. Imagenet large scale visual recognition challenge. *International journal of computer vision*, 115:211–252, 2015.
- Joel Saltz, Rajarsi Gupta, Le Hou, Tahsin Kurc, Pankaj Singh, Vu Nguyen, Dimitris Samaras, Kenneth R Shroyer, Tianhao Zhao, Rebecca Batiste, et al. Spatial organization and molecular correlation of tumor-infiltrating lymphocytes using deep learning on pathology images. *Cell reports*, 23(1):181–193, 2018a.
- Joel Saltz, Rajarsi Gupta, Le Hou, Tahsin Kurc, Pankaj Singh, Vu Nguyen, Dimitris Samaras, Kenneth R Shroyer, Tianhao Zhao, Rebecca Batiste, et al. Spatial organization and molecular correlation of tumor-infiltrating lymphocytes using deep learning on pathology images. *Cell reports*, 23(1):181–193, 2018b.
- Denis Schapiro, Hartland W Jackson, Swetha Raghuraman, Jana R Fischer, Vito RT Zanotelli, Daniel Schulz, Charlotte Giesen, Raúl Catena, Zsuzsanna Varga, and Bernd Bodenmiller. histocat: analysis of cell phenotypes and interactions in multiplex image cytometry data. *Nature methods*, 14(9): 873–876, 2017.
- Zhuchen Shao, Hao Bian, Yang Chen, Yifeng Wang, Jian Zhang, Xiangyang Ji, et al. Transmil: Transformer based correlated multiple instance learning for whole slide image classification. *Advances in neural information processing systems*, 34:2136–2147, 2021.
- Artem Shmatko, Narmin Ghaffari Laleh, Moritz Gerstung, and Jakob Nikolas Kather. Artificial intelligence in histopathology: enhancing cancer research and clinical oncology. *Nature cancer*, 3(9):1026–1038, 2022.

- Abhishek Vahadane, Tingying Peng, Amit Sethi, Shadi Albarqouni, Lichao Wang, Maximilian Baust, Katja Steiger, Anna Melissa Schlitter, Irene Esposito, and Nassir Navab. Structure-preserving color normalization and sparse stain separation for histological images. *IEEE Transactions on Medical Imaging*, 35:1962–1971, 2016. URL <https://api.semanticscholar.org/CorpusID:6994762>.
- Laurens van der Maaten and Geoffrey Hinton. Visualizing data using t-sne. *Journal of Machine Learning Research*, 9(86):2579–2605, 2008. URL <http://jmlr.org/papers/v9/vandermaaten08a.html>.
- Bastiaan S Veeling, Jasper Linmans, Jim Winkens, Taco Cohen, and Max Welling. Rotation equivariant CNNs for digital pathology. June 2018.
- Eugene Vorontsov, Alican Bozkurt, Adam Casson, George Shaikovski, Michal Zelechowski, Siqi Liu, Philippe Mathieu, Alexander van Eck, Donghun Lee, Julian Viret, et al. Virchow: a million-slide digital pathology foundation model. *arXiv preprint arXiv:2309.07778*, 2023.
- Sophia J. Wagner, Nadieh Khalili, Raghav Sharma, Melanie Boxberg, Carsten Marr, Walter de Back, and Tingying Peng. Structure-preserving multi-domain stain color augmentation using style-transfer with disentangled representations. In *Medical Image Computing and Computer Assisted Intervention – MICCAI 2021*, 2021.
- Xiyue Wang, Sen Yang, Jun Zhang, Minghui Wang, Jing Zhang, Wei Yang, Junzhou Huang, and Xiao Han. Transformer-based unsupervised contrastive learning for histopathological image classification. *Medical image analysis*, 81:102559, 2022.
- Jerry Wei, Arief Suriawinata, Bing Ren, Xiaoying Liu, Mikhail Lisovsky, Louis Vaickus, Charles Brown, Michael Baker, Naofumi Tomita, Lorenzo Torresani, et al. A petri dish for histopathology image analysis. In *International Conference on Artificial Intelligence in Medicine*, pages 11–24. Springer, 2021.
- John N Weinstein, Eric A Collisson, Gordon B Mills, Kenna R Shaw, Brad A Ozenberger, Kyle Ellrott, Ilya Shmulevich, Chris Sander, and Joshua M Stuart. The cancer genome atlas pan-cancer analysis project. *Nature genetics*, 45(10):1113–1120, 2013.
- Hanwen Xu, Naoto Usuyama, Jaspreet Bagga, Sheng Zhang, Rajesh Rao, Tristan Naumann, Cliff Wong, Zelalem Gero, Javier González, Yu Gu, Yanbo Xu, Mu Wei, Wenhui Wang, Shuming Ma, Furu Wei, Jianwei Yang, Chunyuan Li, Jianfeng Gao, Jaylen Rosemon, Tucker Bower, Soohee Lee, Roshanthi Weerasinghe, Bill J. Wright, Ari Robicsek, Brian Piening, Carlo Bifulco, Sheng Wang, and Hoifung Poon. A whole-slide foundation model for digital pathology from real-world data. *Nature*, 2024.
- Jiawei Yang, Hanbo Chen, Yuan Liang, Junzhou Huang, Lei He, and Jianhua Yao. Concl: Concept contrastive learning for dense prediction pre-training in pathology images. In *European Conference on Computer Vision*, pages 523–539. Springer, 2022.
- Jure Zbontar, Li Jing, Ishan Misra, Yann LeCun, and Stéphane Deny. Barlow twins: Self-supervised learning via redundancy reduction. *arXiv preprint arXiv:2103.03230*, 2021.
- Jinghao Zhou, Chen Wei, Huiyu Wang, Wei Shen, Cihang Xie, Alan Yuille, and Tao Kong. ibot: Image bert pre-training with online tokenizer. *International Conference on Learning Representations (ICLR)*, 2022.
- Jun-Yan Zhu, Taesung Park, Phillip Isola, and Alexei A. Efros. Unpaired image-to-image translation using cycle-consistent adversarial networks. In *2017 IEEE International Conference on Computer Vision (ICCV)*, pages 2242–2251, 2017. doi: 10.1109/ICCV.2017.244.

## **EXAONEPath AI Model License Agreement 1.0 - NC**

This License Agreement (“Agreement”) is entered into between you (“Licensee”) and LG Management Development Institute Co., Ltd. (“Licensor”), governing the use of the EXAONEPath AI Model (“Model”). By downloading, installing, copying, or using the Model, you agree to comply with and be bound by the terms of this Agreement. If you do not agree to all the terms, you must not download, install, copy, or use the Model. This Agreement constitutes a binding legal agreement between the Licensee and Licensor.

### **1. Definitions**

#### **1.1 Model**

The artificial intelligence model provided by Licensor, which includes any software, algorithms, machine learning models, or related components supplied by Licensor. This definition extends to encompass all updates, enhancements, improvements, bug fixes, patches, or other modifications that may be provided by Licensor from time to time, whether automatically or manually implemented.

#### **1.2 Derivatives**

Any modifications, alterations, enhancements, improvements, adaptations, or derivative works of the Model created by Licensee or any third party. This includes changes made to the Model’s architecture, parameters, data processing methods, or any other aspect of the Model that results in a modification of its functionality or output.

#### **1.3 Output**

Any data, results, content, predictions, analyses, insights, or other materials generated by the Model or Derivatives, regardless of whether they are in their original form or have been further processed or modified by the Licensee. This includes, but is not limited to, textual or numerical produced directly or indirectly through the use of the Model.

#### **1.4 Licensor**

LG Management Development Institute Co., Ltd., the owner, developer, and provider of the EXAONEPath AI Model. The Licensor holds all rights, title, and interest in the Model and is responsible for granting licenses to use the Model under the terms specified in this Agreement.

#### **1.5 Licensee**

The individual, organization, corporation, academic institution, government agency, or other entity using or intending to use the Model under the terms and conditions of this Agreement. The Licensee is responsible for ensuring compliance with the Agreement by all authorized users who access or utilize the Model on behalf of the Licensee.

### **2. License Grant**

#### **2.1 Grant of License**

Subject to the terms and conditions outlined in this Agreement, the Licensor hereby grants the Licensee a limited, non-exclusive, non-transferable, worldwide, and revocable license to:

- a. Access, download, install, and use the Model solely for research purposes. This includes evaluation, testing, academic research and experimentation.
- b. Publicly disclose research results and findings derived from the use of the Model or Derivatives, including publishing papers or presentations.

- c. Modify the Model and create Derivatives based on the Model, provided that such modifications and Derivatives are used exclusively for research purposes. The Licensee may conduct experiments, perform analyses, and apply custom modifications to the Model to explore its capabilities and performance under various scenarios. If the Model is modified, the modified Model must include "EXAONEPath" at the beginning of its name.
- d. Distribute the Model and Derivatives in each case with a copy of this Agreement.

## **2.2 Scope of License**

The license granted herein does not authorize the Licensee to use the Model for any purpose not explicitly permitted under this Agreement. Any use beyond the scope of this license, including any commercial application or external distribution, is strictly prohibited unless explicitly agreed upon in writing by the Licensor.

## **3. Restrictions**

### **3.1 Commercial Use**

The Licensee is expressly prohibited from using the Model, Derivatives, or Output for any commercial purposes, including but not limited to, developing or deploying products, services, or applications that generate revenue, whether directly or indirectly. Any commercial exploitation of the Model or its derivatives requires a separate commercial license agreement with the Licensor. Furthermore, the Licensee shall not use the Model, Derivatives or Output to develop or improve other models, except for research purposes, which is explicitly permitted.

### **3.2 Reverse Engineering**

The Licensee shall not decompile, disassemble, reverse engineer, or attempt to derive the source code, underlying ideas, algorithms, or structure of the Model, except to the extent that such activities are expressly permitted by applicable law. Any attempt to bypass or circumvent technological protection measures applied to the Model is strictly prohibited.

### **3.3 Unlawful Use**

The Licensee shall not use the Model and Derivatives for any illegal, fraudulent, or unauthorized activities, nor for any purpose that violates applicable laws or regulations. This includes but is not limited to the creation, distribution, or dissemination of malicious, deceptive, or unlawful content.

### **3.4 Ethical Use**

The Licensee shall ensure that the Model or Derivatives is used in an ethical and responsible manner, adhering to the following guidelines:

- a. The Model and Derivatives shall not be used to generate, propagate, or amplify false, misleading, or harmful information, including fake news, misinformation, or disinformation.
- b. The Model and Derivatives shall not be employed to create, distribute, or promote content that is discriminatory, harassing, defamatory, abusive, or otherwise offensive to individuals or groups based on race, gender, sexual orientation, religion, nationality, or other protected characteristics.
- c. The Model and Derivatives shall not infringe on the rights of others, including intellectual property rights, privacy rights, or any other rights recognized by law. The Licensee shall obtain all necessary permissions and consents before using the Model and Derivatives in a manner that may impact the rights of third parties.
- d. The Model and Derivatives shall not be used in a way that causes harm, whether physical, mental, emotional, or financial, to individuals, organizations, or communities. The Licensee shall take all reasonable measures to prevent misuse or abuse of the Model and Derivatives that could result in harm or injury.

## **4. Ownership**

### **4.1 Intellectual Property**

All rights, title, and interest in and to the Model, including any modifications, Derivatives, and associated documentation, are and shall remain the exclusive property of the Licensor. The Licensee acknowledges that this Agreement does not transfer any ownership rights to the Licensee. All trademarks, service marks, and logos associated with the Model are the property of the Licensor.

### **4.2 Output**

All output generated by the Model from Licensee Data ("Output") shall be the sole property of the Licensee. Licensor hereby waives any claim of ownership or intellectual property rights to the Output. Licensee is solely responsible for the legality, accuracy, quality, integrity, and use of the Output.

### **4.3 Attribution**

In any publication or presentation of results obtained using the Model, the Licensee shall provide appropriate attribution to the Licensor, citing the Model's name and version, along with any relevant documentation or references specified by the Licensor.

## **5. No Warranty**

### **5.1 "As-Is" Basis**

The Model, Derivatives, and Output are provided on an "as-is" and "as-available" basis, without any warranties or representations of any kind, whether express, implied, or statutory. The Licensor disclaims all warranties, including but not limited to, implied warranties of merchantability, fitness for a particular purpose, accuracy, reliability, non-infringement, or any warranty arising from the course of dealing or usage of trade.

### **5.2 Performance and Reliability**

The Licensor does not warrant or guarantee that the Model, Derivatives or Output will meet the Licensee's requirements, that the operation of the Model, Derivatives or Output will be uninterrupted or error-free, or that defects in the Model will be corrected. The Licensee acknowledges that the use of the Model, Derivatives or Output is at its own risk and that the Model, Derivatives or Output may contain bugs, errors, or other limitations.

### **5.3 No Endorsement**

The Licensor does not endorse, approve, or certify any results, conclusions, or recommendations derived from the use of the Model. The Licensee is solely responsible for evaluating the accuracy, reliability, and suitability of the Model for its intended purposes.

## **6. Limitation of Liability**

### **6.1 No Liability for Damages**

To the fullest extent permitted by applicable law, in no event shall the Licensor be liable for any special, incidental, indirect, consequential, exemplary, or punitive damages, including but not limited to, damages for loss of business profits, business interruption, loss of business information, loss of data, or any other pecuniary or non-pecuniary loss arising out of or in connection with the use or inability to use the Model, Derivatives or any Output, even if the Licensor has been advised of the possibility of such damages.

## **6.2 Indemnification**

The Licensee agrees to indemnify, defend, and hold harmless the Licensor, its affiliates, officers, directors, employees, and agents from and against any claims, liabilities, damages, losses, costs, or expenses (including reasonable attorneys' fees) arising out of or related to the Licensee's use of the Model, any Derivatives, or any Output, including any violation of this Agreement or applicable laws. This includes, but is not limited to, ensuring compliance with copyright laws, privacy regulations, defamation laws, and any other applicable legal or regulatory requirements.

## **7. Termination**

### **7.1 Termination by Licensor**

The Licensor reserves the right to terminate this Agreement and revoke the Licensee's rights to use the Model at any time, with or without cause, and without prior notice if the Licensee breaches any of the terms or conditions of this Agreement. Termination shall be effective immediately upon notice.

### **7.2 Effect of Termination**

Upon termination of this Agreement, the Licensee must immediately cease all use of the Model, Derivatives, and Output and destroy all copies of the Model, Derivatives, and Output in its possession or control, including any backup or archival copies. The Licensee shall certify in writing to the Licensor that such destruction has been completed.

### **7.3 Survival**

The provisions of this Agreement that by their nature should survive termination, including but not limited to, Sections 4 (Ownership), 5 (No Warranty), 6 (Limitation of Liability), and this Section 7 (Termination), shall continue to apply after termination.

## **8. Governing Law**

### **8.1 Governing Law**

This Agreement shall be governed by and construed in accordance with the laws of the Republic of Korea, without regard to its conflict of laws principles.

### **8.2 Arbitration**

Any disputes, controversies, or claims arising out of or relating to this Agreement, including its existence, validity, interpretation, performance, breach, or termination, shall be referred to and finally resolved by arbitration administered by the Korean Commercial Arbitration Board (KCAB) in accordance with the International Arbitration Rules of the Korean Commercial Arbitration Board in force at the time of the commencement of the arbitration. The seat of arbitration shall be Seoul, Republic of Korea. The tribunal shall consist of one arbitrator. The language of the arbitration shall be English.

## **9. Alterations**

### **9.1 Modifications**

The Licensor reserves the right to modify or amend this Agreement at any time, in its sole discretion. Any modifications will be effective upon posting the updated Agreement on the Licensor's website or through other means of communication. The Licensee is responsible for reviewing the Agreement periodically for changes. Continued use of the Model after any modifications have been made constitutes acceptance of the revised Agreement.



## **9.2 Entire Agreement**

This Agreement constitutes the entire agreement between the Licensee and Licensor concerning the subject matter hereof and supersedes all prior or contemporaneous oral or written agreements, representations, or understandings. Any terms or conditions of any purchase order or other document submitted by the Licensee in connection with the Model that are in addition to, different from, or inconsistent with the terms and conditions of this Agreement are not binding on the Licensor and are void.

By downloading, installing, or using the EXAONEPath AI Model, the Licensee acknowledges that it has read, understood, and agrees to be bound by the terms and conditions of this Agreement.